EFFECTS OF THERMAL AND ELECTRICAL PROPERTIES OF THIN METAL FILM IN PHOTOINDUCTIVE FIELD-MAPPING TECHNIQUE FOR EDDY-CURRENT PROBES

Y.-L. Pan[*] and C.-C. Tai

Department of Electrical Engineering, National Cheng Kung University, Tainan 70101, Taiwan

Abstract—Photoinductive (PI) field mapping for eddy-current (EC) probes above a thin metal film was performed by multiphysics analysis with two-dimensional finite element method (FEM). The FEM model of PI method was used to observe how metal film properties affect the field-mapping signals of EC probes. The PI signal was tested for effects of resistivity, temperature coefficient of the resistivity, thermal conductivity, heat capacity, and thin film density The applicability of actual thin film materials for mapping the field of EC probe when using PI method was discussed. Field-mapping signals of EC probe coils with tilt angles of 0°, 5°, 10°, 15°, and 20° were also examined with appropriate metal film material. These experiments showed that the higher-resolution field-mapping signals of EC probes can be obtained by given a titanium thin film The resolution of field-mapping signals of EC probes correlated positively with resistivity, heat capacity, and density of thin film and correlated negatively with its thermal conductivity. Improved understanding of distinct field distribution of EC probes enables selection of optimal probes for EC inspection.

1. INTRODUCTION

In the past fifteen years, photoinductive (PI) imaging has been a novel nondestructive testing (NDT) method of detecting and measuring cracks [1, 2]. It is also an ideal field-mapping technique that provides high spatial resolution and high sensitivity to the tangential component of the electromagnetic field without perturbation when characterizing the electromagnetic field of eddy-current (EC) probes [2–5]. Field-mapping images for commercial EC probes can be obtained by

PI method with a 20-μm thick gold film on an insulating glass substrate [3]. The experimental results obtained by PI field-mapping, however, do not consider the effects of thermal and electrical properties of the thin film, which leads to insufficient data for mapping more distinct field distributions of EC probes.

Studies of the effects of parameters for real conditions of physical systems [5–14] have attempted to optimize physical parameters (e.g., coil current frequency, laser point temperature, lift-off distance, and tilt angle of coil) for enhancing coil probe output signals [6] and preventing the noises to obscure the valuable signals [14]. The electromagnetic field and impedance of a cylindrical eddy-current probe coil are calculated analytically and numerically for arbitrary coil orientation [12–14]. However, the PI method is a multiphysics sensing method that combines ECT and thermal-wave methods. It is difficult to solve the analytical solution of the PI method, and furthermore thin film parameters such as resistivity, temperature coefficient of resistivity, thermal conductivity, heat capacity, and density have not been evaluated in terms of their effects on PI field-mapping results. Therefore, this study applied the proposed FEM model in PI field mapping to visualize and analyze the effects of these five parameters on the field-mapping of an EC probe. The experimental PI results were used to determine the optimal metal film for high-resolution mapping of electromagnetic field distribution in commercial EC probes. These experimental results can also be used to optimize selection of EC inspection probes without tilted coils.

2. THE FEM MODEL OF THE PHOTOINDUCTIVE METHOD

This section describes the FEM model of the effect of the thin metal film properties in the PI field-mapping technique, which the authors proposed earlier in [5]. Figure 1 shows the physical principles of the PI mapping method. The probe, cylinder, and air-cored coils were placed close to a thin metal film supported on an insulating glass substrate and then excited with appropriate voltage and frequency. A laser beam was focused on the bottom of the metal film to introduce variation in temperature and conductivity of the metal foil; moreover, the laser also induced a change in the impedance of the EC probe. Therefore, when the asymmetrical tilted magnetic field was produced by the tilted coil of EC probes, asymmetrical distributions of induced eddy current on the metal film were mapped by the different impedances produced in the EC probe by varying electrical conductivity of the thin film. In addition, instead of the actual coils mounted in the EC probes, a
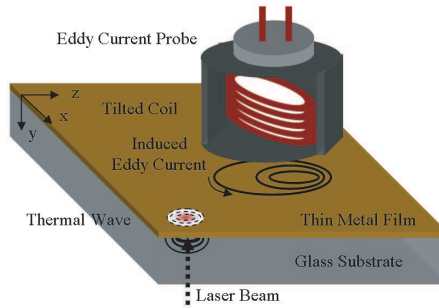
Figure 1. Schematic diagram of the photoinductive field measurement.

simplified one-turn, air-cored coil was used to simplify the calculations. The rectangular coordinate system is used in the following discussion.

2.1. Analysis of Heat Transfer Field

The 2-D simulation assumed a negligible temperature variance T (°C or K) in the z direction of the specimen, i.e., a heat distribution over the x and y directions of the plate. The 2-D transient model for heat transfer by conduction is as follows [15, 16]:

$$\rho C \frac{\partial T}{\partial t} - k \left(\frac{\partial^2 T}{\partial x^2} + \frac{\partial^2 T}{\partial y^2} \right) = Q, \tag{1}$$

where T, ρ, C, k, and Q are the temperature, the density (kg/m^3), the heat capacity (J/[kg · K]), the thermal conductivity (W/[m · K]), and the heat source (W/m^3), respectively. The point heat source of the laser beam, where the delta function of heat source is δ (W/m^3), was used to solve Equation (1). Thin film properties were assumed to depend on the distribution of heat produced by a modulated laser beam for a specified period [2].

2.2. Analysis of Electromagnetic Field

According to the quasi-static analysis for ECT in electromagnetic fields, $\partial \mathbf{D}/\partial t = 0$ is valid in the Ampere law of Maxwell equations. Magnetization and the moving velocity of the geometry were also assumed to be zero. In a 2-D time harmonic analysis, the variation of magnetic field is parallel to the x-y plane while the current of coil probe is perpendicular to the x-y plane In addition, the simplified
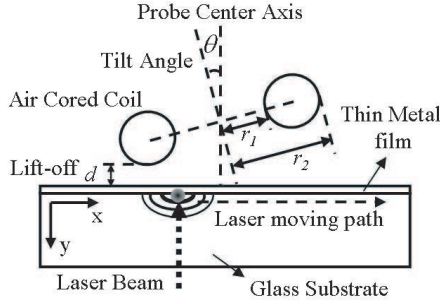
Figure 2. The 2-D model of the PI method for field mapping of EC probe with tilted air-cored coils above a metal foil. A simplified one-turn, air-cored coil was instead of actual coils mounted in the EC probes. The crosssectional view (side view) shows the x-y plane.

one-turn, air-cored coil are treated as two separate segment wires in a 2-D cross-sectional view (as shown in Figure 2). Three subdomains of the electromagnetic field were modeled: air, coil, and metal film (Equations (2)–(4), respectively) [17, 18]

$$\frac{\partial}{\partial x}\left(\frac{1}{\mu}\frac{\partial A_z}{\partial x}\right) + \frac{\partial}{\partial y}\left(\frac{1}{\mu}\frac{\partial A_z}{\partial y}\right) = 0 \tag{2}$$

$$j\omega\sigma_{coil}A_z + \frac{\partial}{\partial x}\left(\frac{1}{\mu}\frac{\partial A_z}{\partial x}\right) + \frac{\partial}{\partial y}\left(\frac{1}{\mu}\frac{\partial A_z}{\partial y}\right) = \sigma_{coil}\frac{\Delta V}{L} \tag{3}$$

$$j\omega\sigma_{film}A_z + \frac{\partial}{\partial x}\left(\frac{1}{\mu}\frac{\partial A_z}{\partial x}\right) + \frac{\partial}{\partial y}\left(\frac{1}{\mu}\frac{\partial A_z}{\partial y}\right) = 0 \tag{4}$$

where A_z denotes the magnetic vector potential (Wb/m) in the z direction. The variables ω, μ, and ΔV are the angular frequency (rad/s), the permeability (Wb/[A $\cdot$ m]) of each subdomain, and the potential difference (V) over the wire length (m), L, of the two separate segment wires. The variables σ_{coil} and σ_{film} are the electrical conductivity of the coil and the metal film, respectively.

The conductivity and permeability of the metal film and coil were affected by the temperature. Since the metal films were nonmagnetic, permeability fluctuations were ignored. Electrical conductivity at temperature T is given by the following expression [17]:

$$\sigma = \frac{1}{\rho} = \frac{1}{[\rho_0(1 + \alpha(T - T_0))]} \tag{5}$$

where T_0 and T are the initial temperature (293 K) and the actual temperature in the sub-domain respectively. The ρ_0 is the resistivity

$(\Omega \cdot m)$ of the metal film at temperature T_0, and α is the temperature coefficient ($1/°C$ or $1/K$) of the resistivity. The initial condition was represented by $T_0 = T$ at $t = 0$.

According to the constitutive relations of electromagnetics, current density $\mathbf{J}_{coil}$ of a coil can be calculated by Equation (6) [17]. Induced current (A), I, in the coil was also calculated by integrating its current density over the cross-sectional area (m^2) of the coil, $\mathbf{s}$, as shown in Equation (7). Impedance (Ohms) of the EC probe was calculated by Ohm law ($Z = \Delta V/I$) For the 2-D field-mapping measurements, the thermal and electrical properties of the thin film determined the magnitude of coil impedance. Normalized processes Equation (8) were performed to clearly exhibit the effect of thin film properties

$$\mathbf{J}_{coil} = \sigma_{coil}\mathbf{E} = -\sigma_{coil}\left(\frac{\Delta V}{L} + j\omega A_z\right) \tag{6}$$

$$\int_{\mathbf{S}} \mathbf{J}_{coil} \cdot d\mathbf{s} = I \tag{7}$$

$$Z_{norm} = \frac{Z}{Z_{ref}} \tag{8}$$

where Z_{norm} and Z_{ref} denotes the coil impedance when normalized and when the laser is focused on the starting point

3. ANALYSIS SCHEME

The thin metal films were 10 mm long and 20 µm thick. Table 1 shows the electrical and thermal parameters for the thin films used in the simulation. The one-turn, air-cored coil (inner radius $r_1 = 0.4$ mm and outer radius $r_2 = 1.2$ mm) was excited with 2-MHz, 5-V alternating voltage. The lift-off distance (d) was 0.4 mm. The coil wire length (L) was 0.5 µm. The temperature of the laser focal spot was 573 K. Figure 2 shows the geometry of the 2-D model for the actual PI method used in [5]. The probe used for 2-D raster scan was fixed in the center of the metal foil whereas the laser beam was moved along the x-axis when performing PI method. The scan range of the mapping field was 4.8 mm with 0.1-mm scanning steps. The commercial FEM software COMSOL Multiphysics^{TM} was used for all simulations.

4. RESULTS AND DISCUSSION

This section presents and compares the simulation results obtained by PI field mapping method for different material parameters.

Table 1. Parameter levels of the thin film used in the simulation.

	Property				
	ρ_0	α	k	ρ	C
Level	$10^{-8}\Omega \cdot m$	$10^{-3}/K$	kg/m^3	J/[kg·K]	W/[m · K]
1	10	1	2000	100	10
2	15	2	4250	200	60
3	20	3	6500	300	110
4	25	4	8750	400	160
5	30	5	11000	500	210
6	35	6	13250	600	260
7	40	7	15550	700	310
8	45	8	17750	800	360
9	50	9	20000	900	410
10	55	10	22250	1000	460

Coil impedance obtained by PI method was compared among varying resistivities, temperature coefficients of the resistivity, thermal conductivities, capacities, and densities of thin film. Figure 3 depicts the distribution of the magnetic field and the diffusion of heat from the laser beam when mapping a tilted 15° air-cored cylindrical coil above a 20-µm thick gold film by PI method. The arrows indicate the flow direction and intensity of the magnetic field. The dark surface color indicates the high temperature. It can be seen that the magnetic field tended to flow asymmetrically towards the tilted side of the coil; moreover, it caused the asymmetrical distributions of induced eddy current on the metal film.

Effects of electrical properties of thin film were compared first. The normalized process is also shown to fully characterize the air-cored coil probe. The thin film was 20 µm thick. Figure 4 depicts the normalized coil impedance for different resistivities. The other conductive film parameters were set to the values of level 5 in Table 2. Notably, the signals had two maximum quantities, and signal amplitude increased as the laser beam moved from the starting point of the scan to the center of the coil probe. The simulation results show that the field characteristics of the air-core coil probe are more distinct at $50 * 10^{-8} - \Omega \cdot m$ (Figure 5). However, normalized impedance peaks at $10 * 10^{-8} - \Omega \cdot m$. Figure 6 shows the normalized coil impedance for different resistivities. As can be seen from this figure, increasing the resistivity decreases the normalized impedance. The curve decays
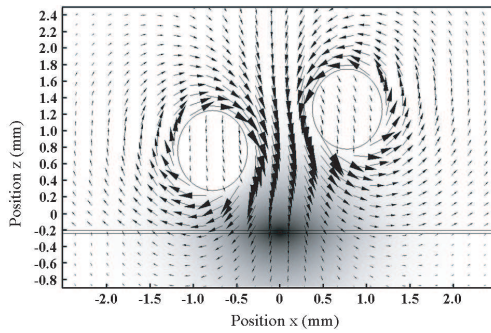
Figure 3. Magnetic field distributions, flow directions, and the heat diffusion from the laser beam above a 20-μm thick gold foil for a tilted 15° air-cored cylindrical coil.
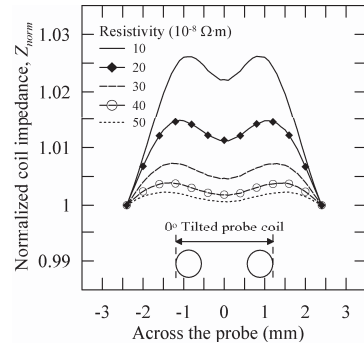
Figure 4. Change in coil impedance obtained by PI mapping method for varying thin film resistivities.

Table 2. Material properties of the air, the probe coil, and thin metal films.

Subdomain	Air	Coil	Thin metal film				
Property	Air	Copper	Au	Ag	Cu	Al	Ti
σ (10^6 S/m)	0	59.98	*	*	*	*	*
ρ_0 ($10^{-8}\Omega \cdot$ m)	*	*	2.24	1.59	1.68	2.65	42
α (10^{-3}/K)	*	*	8.3	6.1	3.9	4.3	2.6
k (W/[m $\cdot$ K])	0.026	401	317	429	401	237	11.4
ρ (kg/m^3)	1.293	8960	19300	10500	8960	2700	4510
C (J/[kg·K])	1.010	384	129	235	384	900	522

Note. The symbol * indicates that the parameter is not used.

fast when the resistivity varies from 10 to 40 and approaches saturation when the resistivity exceeds 40. The cause of this saturation is that the skin depth at a high resistivity tends to increase slowly. Although the normalized amplitude is increased when the low resistivity is applied, the small skin depth results in failure when mapping the field feature for small diameter coils. Therefore, the resistivity of the metal film should be as large as possible for small coils within the EC probe. The relation between coil impedance and resistivity can be approximated by a fourth-order polynomial.

Figure 7 compares the normalized impedance of the PI method for several temperature coefficients for thin film resistivity. It is
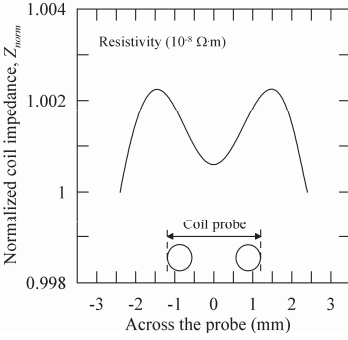
Figure 5. Change in coil impedance in thin film with $50 * 10^{-8}$-$\Omega \cdot$ m resistivity when using PI mapping method.
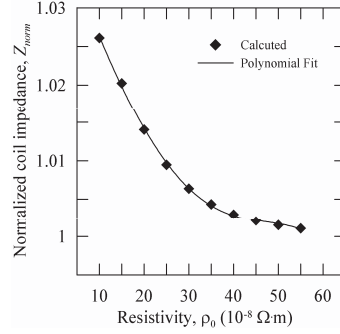

Figure 6. Effect of thin film resistivity on coil impedance when using PI mapping method.
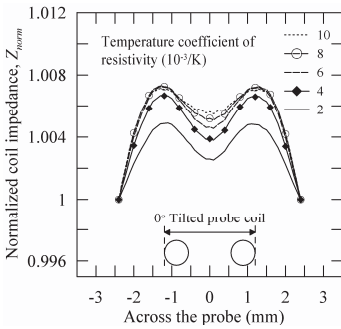

Figure 7. Effect of change in coil impedance for different temperature coefficients of thin film resistivity when using PI.
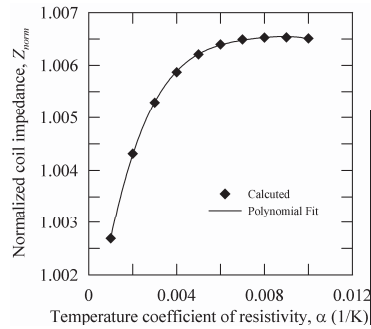

Figure 8. Effect of temperature coefficient of thin film resistivity on coil impedance when using PI mapping method.

shown that the two minimum quantities of normalized impedance occur at 0.002/K. Temperature coefficient of resistivity correlates with resistivity change in the conductive film. High temperature coefficient causes the resistivity of the metal film to be large; thus, variations of normalized impedance tend to stabilize (Figure 8). However, the change of impedance with different temperature coefficients is smaller that with different resistivities. As the results in Figure 7, the field-mapping feature of the air-cored coil also results in similar simulation data for other temperature coefficients of resistivity. Therefore, this parameter is not the key influence factor of field resolution for PI field-
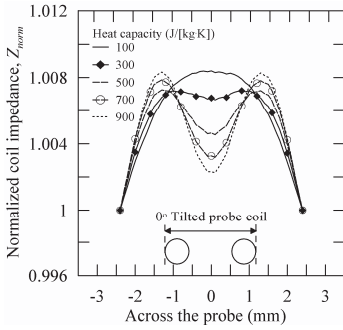
Figure 9. Normalized impedance obtained by PI mapping method for different thin film heat capacities.
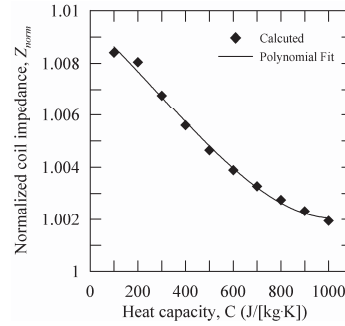
Figure 10. Effect of heat capacity of thin film on coil impedance when using PI mapping method.

mapping method. The simulation data are fitted with a fourth-order polynomial.

Thermal properties of the thin film were then investigated in terms of effects on the field-mapping feature of the air-cored coil. Figures 9 and 11 show that the distinct field-mapping feature of air-cored coil occurs at 900-J/[kg · K] and 20000-kg/m^3. Heat capacity and density clearly affect the field resolution of the PI field-mapping method when comparing signals for different levels of these two parameters. The simulation results in Figures 10 and 12 show that these two parameters correlate negatively with normalized impedance. The reason for this is that decreasing heat capacity and density causes the heat diffuse in the metal film fast; moreover, it is difficult to identify the field characteristics of the air-cored coil due to the high velocity of heat diffusion. Therefore, these two parameters of the film material should be as large as possible in order to clearly characterize the field of EC probes even though the normalized impedance is decreasing. The simulation data were fitted with a fourth-order polynomial.

The above discussion shows that the field-mapping feature of the air-cored coil depends mainly on the speed of temperature change in the thin film. In heat transfer fields, thermal conductivity indicates capability to conduct heat. As we discussed in [6], increased penetration of heat through the specimen increases the peak PI signal. Therefore, normalized impedance was used to identify the field feature of EC coil. Figure 13 shows that the field feature of coil is distinct for a 10-W/[m · K] thermal conductivity of thin film. Although the normalized impedance increased when the high thermal conductivity was applied (Figure 14), the dual-peak field feature of the EC coil
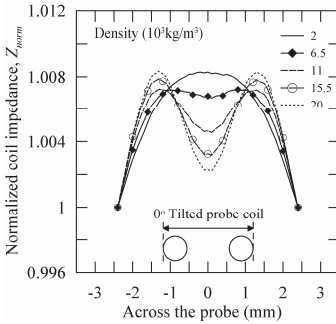
Figure 11. Comparison of normalized impedance mapping in different densities of thin film when using PI mapping method.
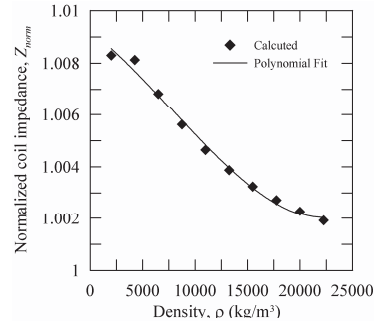

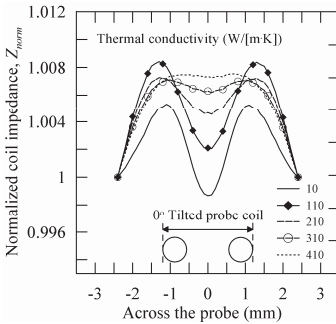**Figure 12.** Effect of thin film density on coil impedance when using PI mapping method.

Figure 13. Comparison of normalized impedance obtained by PI mapping method for different thermal conductivities of thin film.
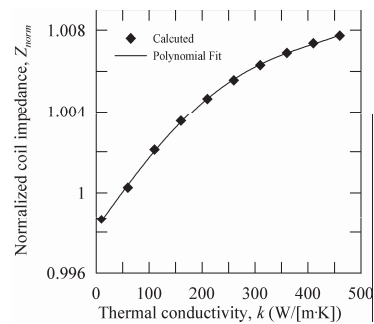

Figure 14. Effect of thermal conductivity of thin film on coil impedance when using PI mapping method.

became more obscure. This condition results in failure when detecting the field variation of the tilted EC coil using PI scanning. The reason for this is that the lower thermal conductivity prevents the heat produced by the laser beam from fully penetrating the thin film from below. Reducing the thermal penetration means that less of the metal volume is affected by the heat from the laser, which causes the more effect in electrical conductivity of the foil. Therefore, the thermal conductivity of the film material should be as small as possible in order to enable mapping of the magnetic field of EC probe with a smaller diameter coil when using PI method. The simulation data are fitted with a fourth-order polynomial.

The above discussion shows that thin film resistivity, thermal conductivity, heat capacity, and density substantially affect the field-mapping feature of coil probe. Therefore, the applicability of actual thin film materials for mapping the field of EC probe when using PI method was investigated next. The actual materials of the metal film were gold (Au), aluminum (Al), titanium (Ti), silver (Ag), and copper (Cu). Table 2 lists the relevant electrical and thermal properties of the metal materials [19]. As noted above, thin film resistivity, heat capacity and density should be as large as possible to clarify the field features of an air-cored coil. Conversely, the thermal conductivity of thin film material should be as small as possible. Titanium is the best material in terms of these criteria. The characteristics of actual coils mounted in the EC probe are the same as the settings of the one-turn, air-cored coil. The tilt angle of the coil within the EC probe was adjusted to be 0°. Figure 15 compares the normalized coil impedance for different actual materials of a 20-μm thick thin film. The actual coils are treated as two rectangular coils in a 2-D cross-sectional view. As expected, titanium film obtains the best enhancement of the dual-peaked field feature of the air-cored coil. In contrast, the gold film obtains the most obscured field distributions of the coil.

In the experimental raster-scanning mode, the 2-D scanning data were converted to a 3-D image of magnetic field of the EC probe Figures 16 and 17 show the 3-D mapping images of the magnetic field of the actual EC probe with a misalignment coil for the gold film and the titanium film. The dark area and low impedance response indicate the week magnetic field produced by the EC probe. The results of the gold film are hard to fully reflect the field feature of EC probe from comparing to that of titanium film. The cause of this condition is
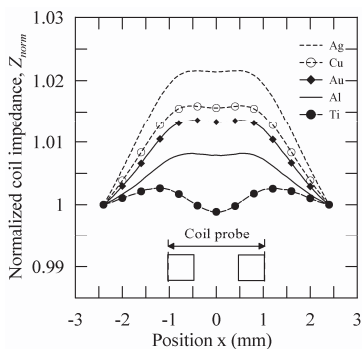

Figure 15. Normalized coil impedance in different foil materials (20-μm thick) used for field mapping of the EC probe with a 0° tilt coil.
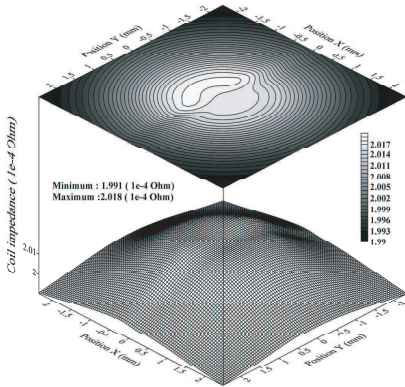
Figure 16. The 3-D surfer plot and 2-D contour plot of mapping the magnetic field of the EC probe with a misalignment coil above a gold film.
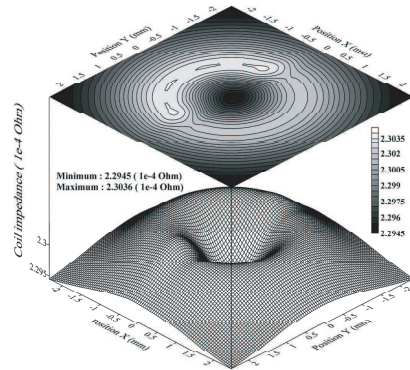
Figure 17. The 3-D surfer plot and 2-D contour plot of mapping the magnetic field of EC probe with a misalignment coil above a titanium film.

that the gold film has much lower resistivity and much higher thermal conductivity than the titanium film. According this experiment, the resistivity and thermal conductivity of thin film are more important impact factors of field-mapping resolution for the PI method. The mapping data are fitted with a fourth-order polynomial.

Figures 18 and 19 show the 1-D magnetic field scans across the diameter of the EC probe with different tilt angles of the EC probe above the gold film and titanium film, respectively. The coil axis of the EC probe was tilted at an angle, θ, from $0°$ to $20°$ with respect to the normal of the metal foil surface. Magnetic interaction clearly weakens as the lift-off distance between the film and the tilted side of coil probe increases, which causes the coil impedance to decrease as the tilted angle of the coil increases. The field feature of the coil above the gold film cannot be identified when the tilted angle is gradually increased. Fortunately, the titanium film minimizes this problem because its electrical and thermal properties decrease heat diffusion in the thin film. The results confirm that the PI method with a titanium film has a high resolution in the field-mapping distribution of the EC probe.
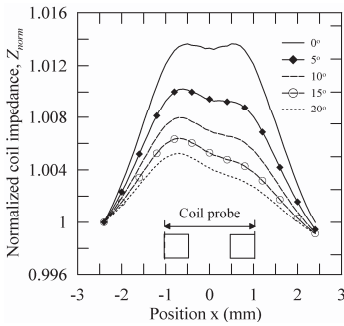
Figure 18. 1-D Magnetic field mapping by PI method with the EC probe at varying coil tilt angles and varying varying coil impedance above a 20-μm thick gold foil.
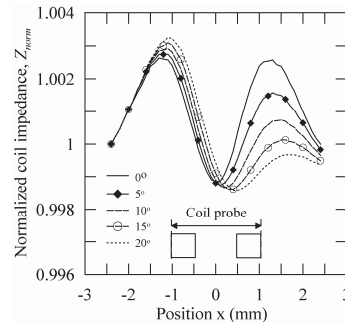
Figure 19. 1-D Magnetic field mapping by PI method with the EC probe at varying coil tilt angles and varying the coil impedance above a 20-μm thick titanium foil.

5. CONCLUSION

This study analyzed the effects of thermal and electrical properties of thin film on the field mapping resolution of EC probes by the FEM technique and demonstrated the clear magnetic field-mapping signals from an actual EC probe can be obtained by PI method with an appropriate foil. Moreover, the resistivity and thermal conductivity of thin film are two critical impact factors of field-mapping resolution for the PI method. It has been shown that a higher normalized impedance is achieved when a smaller resistivity and higher thermal conductivity of the thin film is applied; however, these increased values result in the field-mapping signal becoming obscure for the field feature of the EC coil. Therefore, the resistivity should be raised as far as possible when using PI field-mapping technique whereas thermal conductivity should be lowered. Performing PI method with titanium film conforms to most of these conditions and achieves a field-mapping resolution higher than that of gold film.

Although field-mapping resolution depends largely on the thermal and electrical properties of the thin metal film, further studies are needed to investigate other parameters that are critical to the field-mapping resolution of a commercial EC probe, including laser moving velocity, laser modulated frequency and laser point temperature.

REFERENCES

1. Moulder, J. C., N. Nakagawa, K. S. No, Y. P. Lee, and J. F. McClelland, "Photoinductive imaging: A new nde technique," *Review of Progress in Quantitative Nondestructive Evaluation*, D. O. Thompson and D. E. Chimenti (eds.), 599–611, Plenum Press, New York, 1989

2. Tai, C.-C. and J. C. Moulder, "Bolt-hole corner crack inspection using the photoinductive imaging method," *Journal of Nondestructive Evaluation*, Vol. 19, No. 3, 81–93, 2000.

3. Moulder, J. C. and N. Nakagawa, "Characterizing the performance of eddy current probes using photoinductive field-mapping," *Research in Nondestructive Evaluation*, Vol. 4, No. 4, 221–236, 1992.

4. Nakagawa, N. and J. C. Moulder, "Eddy current probe calibration via the photoinductive effect," *NDT & E International*, Vol. 28, No. 4, 245–246, 1995.

5. Tai, C.-C. and Y.-L. Pan, "Characterizing the performance of eddy current probes using the photoinductive field-mapping: A numerical approach," *International Journal of Applied Science and Engineering*, Vol. 6, No. 3, 215–221, 2009.

6. Tai, C.-C. and Y.-L. Pan, "Multiphysics modeling and analysis of the photoinductive imaging effect for crack detection," *IEEE Transactions on Instrumentation and Measurement*, Vol. 59, No. 2, 425–432, 2010.

7. Mirshekar-Syahkai, D. and R. F. Mostafavi, "Effects of probe and inducer on saturation of crack signal in high-sensitivity ac field measurement technique," *IEE Proceedings Science, Measurement & Technology*, 193–196, 2001.

8. Abakar, A., J.-C. Verite, and R. Cauvin, "Sensitivity analysis of eddy current sensor parameters for non-destructive measurement of zirconium oxide thin film using 3D finite element," *12th Biennial IEEE Conference on Electromagnetic Field Computation*, 426–426, 2006.

9. Singh, S. K., J. P. Pandey, K. B. Thapa, and S. P. Ojha, "Structural parameters in the formation of omnidirectional high reflector," *Progress In Electromagnetics Research*, Vol. 70, 53–78, 2007.

10. O'Halloran, M., M. Glavin, and E. Jones, "Effects of fibroglandular tissue distribution on data-independent beamforming algorithms," *Progress In Electromagnetics Research*, Vol. 97, 141–158, 2009.

11. Zhang, J.-P., Z.-S. Wu, Q.-L. Zhu, and B. Wang, "A four-parameter m-profile model for the evaporation duct estimation from radar clutter," *Progress In Electromagnetics Research*, Vol. 114, 353–368, 2010.

12. Theodoulidis, T., "Analytical model for tilted coils in eddy-current nondestructive inspection," *IEEE Transactions on Magnetics*, Vol. 41, 2447–2454, 2005.

13. Aldrin, J. C. and J. S. Knopp, "Crack characterization method with invariance to noise features for eddy current inspection of fasterner sites," *Journal of Nondestructive Evaluation*, Vol. 25, No. 4, 165–181, 2006.

14. Zhang, Y.-H., F.-L. Luo, and H.-X. Sun, "Impedance evaluation of a probe-coil's lift-off and tilt effect in eddy-current nondestructive inspection by 3D finite element modeling," *17th World Conference on Nondestructive Testing*, 2008.

15. Taine, J. and J. P. Petit, *Heat Transfer*, Prentice Hall, New York, 1993.

16. Lewis, R. W., K. Morgan, H. R. Thomas, and K. N. Seetharamu, *The Finite Element Method in Heat Transfer Analysis*, John Wiley & Sons, Chichester, 1996.

17. Cheng, D. K., *Field and Wave Electromagnetics*, Addison-Wesley, Redwood City, 1989.

18. Jianming, J., *The Finite Element Method in Electromagnetics*, John Wiley & Sons, New York, 2002.

19. Lide, D. R., *Crc Handbook of Chemistry and Physics*, CRC Press, Boca Raton, 2006.